This paper is published as part of a *PCCP* themed issue on solid state and cluster structure prediction

Guest Editors: Richard Catlow and Scott M. Woodley

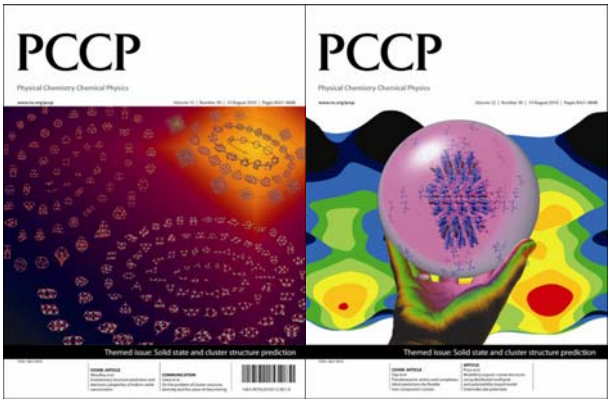

Editorial

Solid state and cluster prediction
Scott M. Woodley and Richard Catlow, *Phys. Chem. Chem. Phys.*, 2010
DOI: 10.1039/c0cp90058c

Communication

On the problem of cluster structure diversity and the value of data mining
Alexey A. Sokol, C. Richard A. Catlow, Martina Miskufova, Stephen A. Shevlin, Abdullah A. Al-Sunaidi, Aron Walsh and Scott M. Woodley, *Phys. Chem. Chem. Phys.*, 2010
DOI: 10.1039/c0cp00068j

Papers

Evolutionary structure prediction and electronic properties of indium oxide nanoclusters
Aron Walsh and Scott M. Woodley, *Phys. Chem. Chem. Phys.*, 2010
DOI: 10.1039/c0cp00056f

Exploration of multiple energy landscapes for zirconia nanoclusters
Scott M. Woodley, Said Hamad and C. Richard A. Catlow, *Phys. Chem. Chem. Phys.*, 2010
DOI: 10.1039/c0cp00057d

Pseudoracemic amino acid complexes: blind predictions for flexible two-component crystals
Carl Henrik Görbitz, Bjørn Dalhus and Graeme M. Day, *Phys. Chem. Chem. Phys.*, 2010
DOI: 10.1039/c004055j

Modelling organic crystal structures using distributed multipole and polarizability-based model intermolecular potentials
Sarah L. Price, Maurice Leslie, Gareth W. A. Welch, Matthew Habgood, Louise S. Price, Panagiotis G. Karamertzanis and Graeme M. Day, *Phys. Chem. Chem. Phys.*, 2010
DOI: 10.1039/c004164e

Ab initio prediction of low-temperature phase diagrams in the Al–Ga–In–As system, MAs–M´As (M, M´= Al, Ga or In) and AlAs–GaAs–InAs, *via* the global study of energy landscapes
Ilya V. Pentin, J. Christian Schön and Martin Jansen, *Phys. Chem. Chem. Phys.*, 2010
DOI: 10.1039/c004040c

Importance of London dispersion effects for the packing of molecular crystals: a case study for intramolecular stacking in a bis-thiophene derivative
Jonas Moellmann and Stefan Grimme, *Phys. Chem. Chem. Phys.*, 2010
DOI: 10.1039/c003432k

An extensive theoretical survey of low-density allotropy in silicon
Martijn A. Zwijnenburg, Kim E. Jelfs and Stefan T. Bromley, *Phys. Chem. Chem. Phys.*, 2010
DOI: 10.1039/c004375c

Predicting transition pressures for obtaining nanoporous semiconductor polymorphs: oxides and chalcogenides of Zn, Cd and Mg
Winyoo Sangthong, Jumras Limtrakul, Francesc Illas and Stefan T. Bromley, *Phys. Chem. Chem. Phys.*, 2010
DOI: 10.1039/c0cp00002g

Databases of virtual inorganic crystal structures and their applications
Armel Le Bail, *Phys. Chem. Chem. Phys.*, 2010
DOI: 10.1039/c003907c

Flexibility of ideal zeolite frameworks
V. Kapko, C. Dawson, M. M. J. Treacy and M. F. Thorpe, *Phys. Chem. Chem. Phys.*, 2010
DOI: 10.1039/c003977b

Constant pressure molecular dynamics simulations for ellipsoidal, cylindrical and cuboidal nano-objects based on inertia tensor information
Clive Bealing, Giorgia Fugallo, Roman Martoňák and Carla Molteni, *Phys. Chem. Chem. Phys.*, 2010
DOI: 10.1039/c004053c

Appearance of bulk-like motifs in Si, Ge, and Al clusters
Wen-Cai Lu, C. Z. Wang, Li-Zhen Zhao, Wei Zhang, Wei Qin and K. M. Ho, *Phys. Chem. Chem. Phys.*, 2010
DOI: 10.1039/c004059b

Small germanium sulfide clusters: mass spectrometry and density functional calculations
Joseph J. BelBruno and Andrei Burnin, *Phys. Chem. Chem. Phys.*, 2010
DOI: 10.1039/c003704d

Prediction of the structures of free and oxide-supported nanoparticles by means of atomistic approaches: the benchmark case of nickel clusters
Giulia Rossi, Luca Anghinolfi, Riccardo Ferrando, Florin Nita, Giovanni Barcaro and Alessandro Fortunelli, *Phys. Chem. Chem. Phys.*, 2010
DOI: 10.1039/c003949g

Crystal structure prediction and isostructurality of three small organic halogen compounds
Aldi Asmadi, John Kendrick and Frank J. J. Leusen, *Phys. Chem. Chem. Phys.*, 2010
DOI: 10.1039/c003971c

Aspects of crystal structure prediction: some successes and some difficulties
Michael O'Keeffe, *Phys. Chem. Chem. Phys.*, 2010
DOI: 10.1039/c004039h

Nanopolycrystalline materials; a general atomistic model for simulation
Dean C. Sayle, Benoît C. Mangili, David W. Price and Thi X. Sayle, *Phys. Chem. Chem. Phys.*, 2010
DOI: 10.1039/b918990d

Isomorphism between ice and silica
Gareth A. Tribello, Ben Slater, Martijn A. Zwijnenburg and Robert G. Bell, *Phys. Chem. Chem. Phys.*, 2010
DOI: 10.1039/b916367k

Investigation of the structures and chemical ordering of small Pd–Au clusters as a function of composition and potential parameterisation
Ramli Ismail and Roy L. Johnston, *Phys. Chem. Chem. Phys.*, 2010
DOI: 10.1039/c004044d

Predicting crystal structures *ab initio*: group 14 nitrides and phosphides
Judy N. Hart, Neil L. Allan and Frederik Claeyssens, *Phys. Chem. Chem. Phys.*, 2010
DOI: 10.1039/c004151c

Zeolitic polyoxometalates metal organic frameworks (Z-POMOF) with imidazole ligands and ε-Keggin ions as building blocks; computational evaluation of hypothetical polymorphs and a synthesis approach
L. Marleny Rodriguez Albelo, A. Rabdel Ruiz-Salvador, Dewi L. Lewis, Ariel Gómez, Pierre Mialane, Jérome Marrot, Anne Dolbecq, Alvaro Sampieri and Caroline Mellot-Draznieks, *Phys. Chem. Chem. Phys.*, 2010
DOI: 10.1039/c004234j

Evolutionary structure prediction and electronic properties of indium oxide nanoclusters

Aron Walsh and Scott M. Woodley*

Received 29th March 2010, Accepted 21st June 2010
First published as an Advance Article on the web 5th July 2010
DOI: 10.1039/c0cp00056f

Indium sesquioxide is widely used as a transparent conducting oxide in modern optoelectronic devices; the rising cost of indium has generated interest in the nanoscale properties of In_2O_3, and questions arise as to the nature of its physicochemical properties below the bulk regime. We report the stable and metastable stoichiometric clusters of $(In_2O_3)_n$, where $n = 1$–10, as predicted from an evolutionary search within the classical interatomic potential and quantum density functional energy landscapes. In contrast to the paradigm set by ZnO, which favours high symmetry bubble-like structures, the In_2O_3 nanoclusters are found to tend towards dense, low symmetry structures approaching the bulk system at remarkably small molecular masses. Electronic characterisation is performed at the hybrid density functional and many-body GW levels to obtain accurate predictions of the spectroscopic properties, with mean values of the ionisation potentials and electron affinities calculated as 7.7 and 1.7 eV, respectively.

1. Introduction

Transparent conducting metal oxides (TCOs) are of immense technological importance,[1] being fundamental components in devices ranging from solar cells to flat-panel displays. While many n-type TCOs are known, *e.g.* ZnO, CdO and SnO_2, the most widely used material is In_2O_3 due to its combination of a large optical band gap and low electrical resistivity.[1–3] The rising cost of indium metal has resulted in the search for viable unconventional TCOs materials with reduced indium content, *e.g.* multi-component oxide solid solutions of Zn, Al, Ga and In.[4–7]

An alternative approach to lower indium content is the utilisation of nanostructures, and these have the potential for offering unique optoelectronic properties. Experimental work in this direction has resulted in the synthesis and characterization of In_2O_3 nanoparticles, crystals, cubes and islands,[8–11] with size distributions ranging from 2 to 60 nm in diameter. In the work of Murali *et al.*,[11] 2–15 nm In_2O_3 nanoparticles were found to adopt bulk-like structures; Lee *et al.*[12] prepared 10 nm nanocubes, while Narayanaswamy *et al.* recently demonstrated the ability to control nanocrystal morphologies ranging from 5 to 60 nm through manipulation of the synthetic route.[9] These studies highlight the strong potential for exploiting In_2O_3 at the nanoscale.

The difficulty in structure and property characterisation below 5 nm presents an ideal opportunity for theoretical guidance and prediction. In this regime, strong deviations are expected from bulk-like local coordination and quantum confinement effects will be greatly enhanced. We report a theoretical search of the nanostructure energy landscape for In_2O_3 using a combination of classical interatomic potentials and density functional theory together with an efficient and robust evolutionary algorithm. The availability and experience of using our own developed software influenced our choice to use the evolutionary algorithm implemented within the GULP code.[13] However, other implementations of genetic algorithms, or indeed other approaches based on simulated annealing or basin hopping, could have been used; for more details and references on other approaches see ref. 14. Stable and metastable stoichiometric clusters for sizes up to $(In_2O_3)_{10}$ are presented: due to the high cation charge and large size, clusters above $(In_2O_3)_6$ are found to favour low symmetry structures approaching those of the bulk material. The results suggest that bulk-like clusters should begin to form at particularly low molecular weights. Assessment of the spectroscopic properties of the global minimum structures within the many body GW formalism show a weak size dependence of the ionisation potential ($\overline{IP} = 7.7$ eV), while the calculated electron affinity varies from 0.7 eV to 2.1 eV ($\overline{EA} = 1.7$ eV); quasiparticle corrections to the single particle eigenvalues are found to most strongly influence the electron affinity.

2. Calculation methodology

To predict the lowest energy clusters formed from stoichiometric $(In_2O_3)_n$ units, we employ an evolutionary algorithm (EA) technique,[14] implemented in the GULP package,[15] which has been successfully applied to ZnO[16] and TiO_2[17] and other clusters based on ionic materials.[18] In brief, thirty candidates, starting from randomized starting configurations, compete both to procreate (thirty children structures are created in each EA cycle) and to survive into the next cycle (population). A Lamarckian version of the EA is used, *i.e.* structures generated in each of the 1000 cycles are subject to local optimisation, where both local minimum and saddle points on the energy surface are generated. Survival into the next EA cycle is based purely on the energies of the relaxed clusters;

University College London, Department of Chemistry, Materials Chemistry, Third Floor, Kathleen Lonsdale Building, Gower Street, London, WC1E 6BT, United Kingdom. E-mail: scott.woodley@ucl.ac.uk

the best unique (structures with a total energy less than 0.001 eV per cluster higher than another are killed off) thirty. For each cluster size, the EA is used ten times, each initiated with a different random seed and in the final, or 1001st, population of each run, we found the global minimum structure.

Throughout the application of the EA, clusters are constrained to be within a spherical container of 16.0 Å diameter. Ten randomised clusters are added to the population on each cycle and procreation is a process of applying a phenotype crossover and mutation (self-crossover or atom exchange).[17,19,20] More precisely, in our crossover process the two parent cluster configurations are rotated by a random angle about a random axis, then the first is cut (along a plane) into two fragments. A similar cut is made to the second parent so that the fragments are composed of the same number and stoichiometry as created from the first parent. Two new clusters, children, are then formed by joining one fragment from each parent (a left part from one parent and a right part from the second, and *vice versa* for the other child). In our mutation process, atom exchange is simply exchanging a random number of atoms in the selected cluster, whereas self crossover occurs by selecting the same cluster to be both parents in our crossover process—note that a different rotation is applied to the clone, otherwise the configuration would not change. The potential barrier,

$$V(r_i) = 50(1 - \tanh[100(r_i - 8.0)]), \qquad (1)$$

defines the edge of the spherical container, where r_i is the distance of atom i from the centre of the container. When generating a new random cluster, atoms are placed on a uniform Cartesian grid, with a spacing of $\sim$0.78 Å, such that no two atoms are on the same grid point within the container.

For the evolutionary search, each In and O ion is represented as a rigid ion with a point charge of $+3|e|$ and $-2|e|$, respectively, and the analytical interatomic potential

$$V(r_{ij}) = \frac{q_i q_j}{r_{ij}} + \frac{A}{r_{ij}^{12}} + B\exp(-r_{ij}/\rho) - \frac{C}{r_{ij}^{6}} \qquad (2)$$

is used to model the interaction between ion i and j, which are distance r_{ij} apart. The first term is simply the Coulomb contribution (in eV) between point charges q_i and q_j, and the latter terms are the standard Lennard-Jones and Born-Mayer terms. For the rigid ion model, the energy of formation is simply the sum of all two body interactions defined by eqn (1). During the evolutionary search we have included the r^{-12} term to penalise interaction distances that are less than a typical bond length (A = 1.0 eV Å^{12} for like charged species and 10.0 eV Å^{12} otherwise). The values for B and C are taken from our earlier work where we modelled various bulk phases for In_2O_3.[21] Note that in our previous work, the shell model[22] was employed to represent electronic polarisation of oxygen. Here, configurations in the final population of the evolutionary algorithm are further refined using the shell model, as defined in ref. 21. As shown in Fig. 1, the ten lowest energy candidate structures, as measured by the energy of formation using the rigid ion and the shell models, were then subject to geometric minimisation using density functional theory (DFT) calculations in the VASP package.[23,24] The exchange–correlation functional of Perdew–Burke–Ernzerhof (PBE)[25] was used within a plane-wave basis set (500 eV) and a projector-augmented wave, scalar-relativistic, core potential (In[Kr]; O[He]).[26]

Due to the inherent complexity of the energy landscape, particularly for larger n, we cannot rely on the ranking of minima, from lowest energy upwards, to be exactly the same on each landscape. Thus, as well as the global minima and the

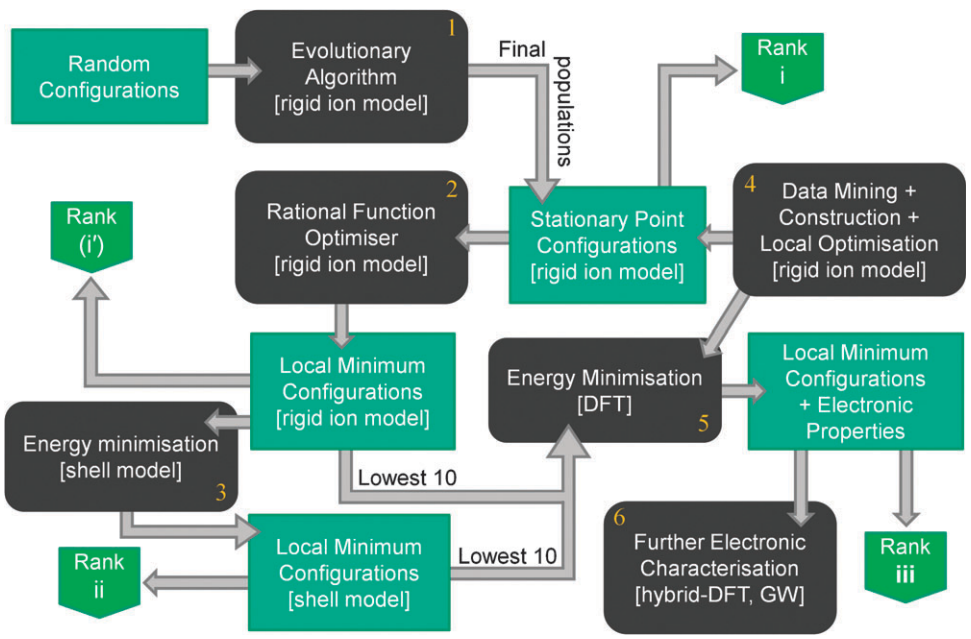

Fig. 1 Schematic of how $(In_2O_3)_n$ clusters with rank i(i′)-ii-**iii** are found. Note that rectangles represent inputs/outputs of the codes GULP (sections 1 to 4), VASP (5), FHI-AIMS (6) and Materials Studio (4).

next nine lowest metastable configurations per cluster size (as measured by the shell model), we also investigated low energy $(A_2B_3)_n$ configurations that have been reported elsewhere. These additional structures, if not already considered as part of either "top ten" (input from below sections 2 and 3 in Fig. 1), were initially constructed using a combination of the visualiser in Materials Studio and energy minimisations using GULP (section 4 in Fig. 1), and, moreover, were always found to be higher local stationary points.

Further electronic characterisation was performed on the global minimum structures identified from the density functional energy landscape, using an all-electron DFT method with a local numerical orbital basis set, as implemented in the FHI-AIMS code.[27,28] A "Tier-2" basis set was employed with scalar-relativistic effects treated at the scaled ZORA level.[29] In addition to the PBE functional, the hybrid PBE0 functional, which replaces 25% of the PBE electron exchange with exact Hartree–Fock exchange[30] was used, where the effective exchange–correlation functional becomes

$$E_{xc}^{PBE0} = E_c^{PBE} + \tfrac{3}{4}E_x^{PBE} + \tfrac{1}{4}E_x^{HF}. \quad (3)$$

Finally, quasiparticle corrections to the PBE0 Kohn–Sham eigenvalues (ε_n^{PBE0}) were included through the G_0W_0 approximation,[31,32] which combines the single-particle Green's function (G) with the dynamically screened Coulomb interaction (W). The resulting quasiparticle energies (E_n^{QP}) emerge as a first-order perturbation,

$$E_n^{QP} \approx \varepsilon_n^{PBE0} + \langle\psi_n|G_0W_0(\varepsilon_n^{PBE0} - V_{xc}^{PBE0})|\psi_n\rangle, \quad (4)$$

and have a direct correspondence with photoemission ($N - 1$ states) and inverse photoemission ($N + 1$ states), or in the case of the HOMO and LUMO levels of the nanoclusters of interest, measures of the respective ionisation potentials and electron affinities. The GW approximation has had recent successes in describing both the band structure and defect properties of metal oxide systems.[33,34]

3. Results and discussion

(a) Energy landscape

The stable, metastable and a number of saddle point structures for $(In_2O_3)_n$, $n = 1$ to 10, are shown in Fig. 2. The configurations are each labelled by their respective point symmetry and rank (energetic ordering, where 0 refers to the global minimum structure for cluster size n), as assessed by the rigid ion, shell and DFT models (see Fig. 1). For example, the last cluster in Fig. 2 is labelled 8-1-**2** C_1, indicating that the cluster has C_1 symmetry, it corresponds to the 8th lowest metastable minimum on the landscape in which the evolutionary algorithm searched, and, upon further refinement using the shell model and then DFT, was found to be the lowest and then the second lowest metastable $In_{20}O_{30}$ configuration. Where there are configurations in the final population of the evolutionary algorithm that correspond to saddle points on the energy landscape, we have ranked the clusters twice; including and excluding (rank given in parenthesis) saddle point structures. For each cluster there are potentially three different relaxed configurations, one configuration originally obtained by the evolutionary algorithm and refined configurations using the different energy functions (shell model and DFT). Typically the relaxed structures for each configuration are similar. If more than one rigid ion structure relaxes to the same local minimum, both are ranked the same but the rigid ion structure that is least like the refined configuration is labelled using a grey font. In Fig. 2 we chose to show only relaxed rigid ion structures as found by our evolutionary algorithm, apart from two relaxed shell model structures that were both better ranked as a result of a change in their symmetry point group and sufficiently different to any initial configuration (rigid ion model). One such example is that found for $n = 1$. The linear stick (symmetry point D_∞) refines to a "flying gull" with a lower symmetry of C_{2v} and non-180° bond angles given in Table 1. Remarkably, the geometrical parameters of this global minimum both for the shell and DFT models are very similar. Upon refinement of the other two configurations found for $n = 1$, using either the shell or DFT approach, the point symmetry did not change, but the energetic ordering did; the bubble D_{3h} configuration is the second lowest energy minimum as assessed using the rigid ion model and the third for the shell and DFT models. Comparing their geometric parameters given in Table 1, there is better agreement between the shell and DFT models, for example the In–O–In bond angle in the bubble cluster is larger than O–In–O for the rigid ion model and smaller for the other two models. Thus, when using our chosen DFT model, less refinement is required if the initial configuration is that found for the shell model (as opposed to the rigid ion model). In fact the agreement between our interatomic potential models and DFT is expected to improve with cluster size since the latter were refined to reproduce the structure and properties of the bulk phase, bixbyite.

The $n = 1$ bubble is the first of a series of perfect bubble structure types, where each bubble has three coordinated indium atoms and two coordinated oxygen atoms. They all have high symmetry, for example, D_{3h}, T_d, D_{3h} and O_h for $n = 1$ to 4; see configurations within blue boxes in Fig. 2. For many binary 1–1 compounds, like ZnO, bubble structures (where all atoms have a coordination number of three) are

Table 1 Bond lengths InX–OY (Å), bond angles (°) and point symmetry for the smallest clusters (flying-gull, linear stick, tetragon-stick, bubble) of In_2O_3, where X and Y are the In and O coordination numbers, respectively

	Point symmetry	Rigid ion	Shell	DFT
In2–O1	C_{2v}	—	1.873	1.848
In2–O2	C_{2v}	—	1.903	1.956
O1–In2–O2	C_{2v}	—	178.5	173.5
In2–O2–In2	C_{2v}	—	151.6	139.5
In2–O1	D_∞	1.642	—	1.849
In2–O2	D_∞	1.872	—	1.938
O–In2–O	D_∞	180.0	—	180.0
In2–O2	C_{2v}	1.772	1.968	2.040
In3–O2	C_{2v}	2.082	2.230	2.105
In3–O1	C_{2v}	1.687	1.892	1.926
In2–O2–In3	C_{2v}	102.9	84.1	90.0
O2–In3–O1	C_{2v}	145.1	136.0	135.8
In3–O2	D_{3h}	1.937	2.111	2.140
In3–O2–In3	D_{3h}	82.4	68.3	77.8
O2–In3–O2	D_{3h}	81.3	91.5	84.8

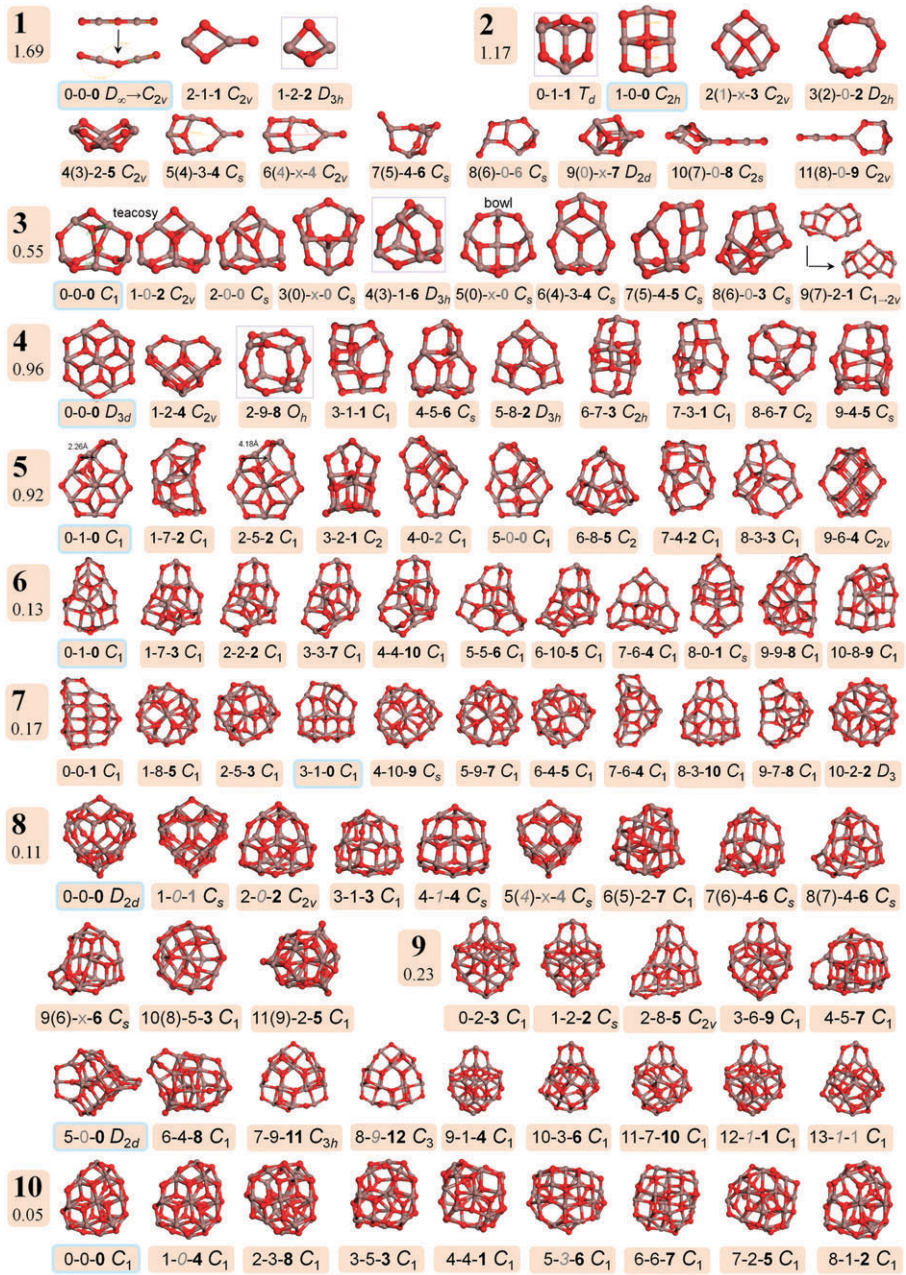

Fig. 2 Stable, metastable and saddle point structures of $(In_2O_3)_n$ nanoclusters, n = 1 to 10, arranged by size n and the initial rank (used during the evolutionary search). The label "i-ii-**iii** X" indicates the rank, as assessed by three different energy functions (rigid ion, shell model, density functional theory), and the point symmetry (as determined by Materials Studio) of the cluster. Numbers in parenthesis do not include saddle points; grey font (or x) indicates that the cluster relaxed to a different (or unphysical) configuration; blue boxes enclosing a configuration or label indicate a perfect bubble or DFT global minima, respectively. The spread in DFT energies (eV/n) for each cluster size is also shown under the main index. Cations are coloured grey with anions coloured red.

predicted to be more stable, particularly those of high symmetry.[16] We note that in our previous study of 2–3 oxides, we found that perfect bubbles become less stable for larger cations.[35] Moreover, the cations in perfect bubbles for 2–3 compounds are spaced further apart compared to the 1–1 bubbles and are more likely to be less stable, particularly for larger size clusters, *i.e.* the bubble is likely to collapse, or fold in, in order to lower its total energy. Note that we predict that the rank in stability of the perfect $(In_2O_3)_n$ bubbles drops with size; rank as assessed by DFT is 1, 6, 8 and >10 for n = 2, 3, 4 and >4 (where rank 0 indicates the global minimum structure). Perfect bubble clusters for $(Al_2O_3)_n$ have been predicted to be the global minima from a limited structure set (as assessed by DFT at the B3LYP/6-31G(d,p) level) for sizes n = 1 to 5.[36] For larger n, alumina clusters formed from more than one smaller bubble (see analogous india clusters in Fig. 3) were found to be more stable than the perfect bubbles.[36] For $(Fe_2O_3)_n$, the perfect bubble was predicted to be the global minimum (DFT B3LYP) for n = 2; larger than this and similar multi-bubbles are found to be more stable (the lowest

energy configuration for $(Fe_2O_3)_5$ is formed from $n = 2$ and 3 perfect bubbles).[37]

Another way to stabilise bubble structures for 2–3 compounds is to allow for higher coordination so that a disc-shaped bubble is formed, for example, $n = 4$ clusters 0-0-**0** and 5-8-**2**, which have higher curvature where indium atoms are four coordinated and oxygen two, and lower curvature where atoms are three coordinated to form hexagons. As with the perfect zinc oxide bubbles, these contain a minimum number of tetragons (six, when only composed of tetragonal and hexagonal faces). Open bubbles, which contain larger faces (octagonal, decagonal,...) appear in the lowest energy configurations for smaller clusters; the lowest three structures for $n = 3$ found by our evolutionary algorithm have an octagonal bottom face (as viewed in Fig. 2) and resembles a tea-cosy. The "tea-cosy" with C_1 point symmetry is the $(In_2O_3)_3$ DFT global minimum, and the more symmetric variant with C_{2v} symmetry is the third lowest minimum (a bowl shape configuration, 9(7)-2-**1**, is our second lowest DFT minimum). These two "tea-cosy" configurations are also predicted to be the lowest energy configurations for $(Fe_2O_3)_3$.[37] With a higher ratio of anions than that of 1–1 compounds, rather than spacing the cations furthest apart, excess anions can occupy sites within or outside a 1–1 bubble, thus becoming denser. Although the DFT global minimum structures for $n = 7$ and 8 have D_{2d} symmetry, many of the larger, low energy, $(In_2O_3)_n$ clusters are dense-like particles and typically they have low symmetry (C_1). Moreover, unlike 1–2 compounds (titania[38] or zirconia),[39] singly coordinated atoms are not found in any of the india clusters shown in Fig. 2 for $n > 2$.

(b) Cluster stability

The formation enthalpies of the nanoclusters relative to the bulk bixbyite phase of In_2O_3 are shown in Fig. 4, as calculated from

$$E_f^{\text{Cluster}} = \left(\frac{E^{\text{Cluster}} - nE^{\text{Bulk}(In_2O_3)}}{n} \right). \qquad (5)$$

The cluster stability rapidly increases with increasing cluster size for each of the three energy landscapes. The cluster energies in both the rigid ion and shell models follow the same overall trend as the DFT landscape, but the individual clusters are significantly

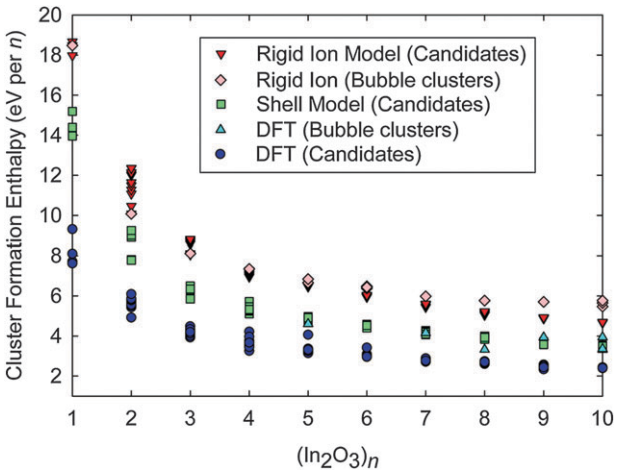

Fig. 4 The cluster formation enthalpies (per formula unit) relative the thermodynamically stable bulk bixbyite phase of In_2O_3 (at 0 eV) from three levels of theory. The candidate clusters refer to those that emerged from global optimisation, while the bubble clusters were considered separately.

higher in energy. This can be accounted for by considering that the potential models were fit to reproduce the bulk phase, and the smaller bond lengths caused by the increased Coloumbic attraction between ions will be penalised by the short-range potential. The addition of shell polarisation to the rigid ion model draws the energies closer to the DFT values. Therefore, while the DFT methods offer an unbiased description of the bulk and nanoscale systems, a qualitatively similar energy profile is produced in each case, especially when polarisation effects are explicitly included. The cluster stabilities increase as a function, $\Delta E_f \propto \frac{1}{\sqrt{n}}$, which is expected to dampen to $\frac{1}{\sqrt{3}}$ above $n = 10$, based on the behaviour of ZnO and SiO_2 nanoclusters.[18] For both the IP and the DFT landscapes, the perfect bubble clusters and multiple bubble clusters, as shown in Fig. 3, form a distinct band split off from the main candidate clusters, lying higher in energy for each case. In fact, of these clusters, the perfect bubble clusters greater than $n = 6$ are higher in energy than the clusters constructed of smaller bubbles, including the onion bubble for $n = 10$, which is found to be even less stable than the two $n = 5$ perfect bubbles that are joined to form a barrel with D_{5d} symmetry.

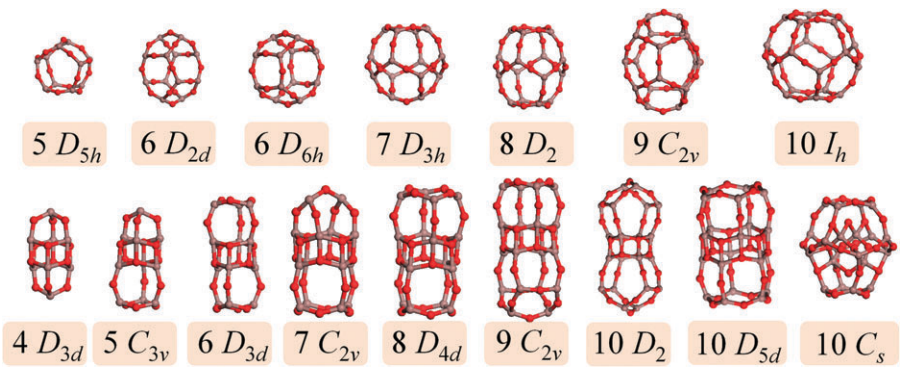

Fig. 3 Perfect bubble clusters (top) and clusters constructed from smaller bubble clusters (bottom) for $(In_2O_3)_n$, where grey and red spheres represent the cations and anions, respectively. Labels indicate the size, n, and the point symmetry of the clusters (as determined by Materials Studio).

(c) Structural characterisation

To quantitatively compare the indium coordination environments between different candidate clusters, we adopt the effective coordination number (ECN) approach of Hoppe *et al.*,[40] which takes into account the number of oxygen ions around a given indium, where the individual bond distances l_i are weighted according to the average distance l_{av}:

$$\mathrm{ECN} = \sum_i \exp\left(1 - \left(\frac{l_i}{l_{av}}\right)^6\right). \quad (6)$$

The average indium–oxygen separation is itself calculated with respect to the minimum indium–oxygen separation (l_{min}):

$$l_{av} = \frac{\sum_i l_i \exp\left(1 - \left(\frac{l_i}{l_{min}}\right)^6\right)}{\sum_i \exp\left(1 - \left(\frac{l_i}{l_{min}}\right)^6\right)}. \quad (7)$$

For an ideal polyhedron, the integer coordination number is reproduced, *e.g.* in the bulk bixbyite phase of In_2O_3, the ECN for the two unique In sites is 5.89 and 6.00, representative of the distorted In–O octahedra with small variation in the bond lengths.[41] To quantitatively assess the differences in coordination, we have plotted the ECN of each candidate cluster in Fig. 5. While for $n = 1$, linear coordination (ECN = 2) is preferred, for larger molecular masses ($n > 3$), a clear trend emerges towards favouring higher coordination numbers. Due to the small cluster sizes, a large proportion of the indium sites are associated with surface sites with inherently reduced coordination; however, the preference for dense low symmetry clusters allows for an increase to ECN greater than 4 for larger cluster sizes.

(d) Electronic characterisation

Analysis of their electronic states reveals that each of the identified stable and metastable structures have finite HOMO–LUMO separations, with the highest energy occupied states being dominated by O 2*p* and the lowest lying empty states consisting largely of In 5*s* and 5*p* orbitals. The density functional calculations are therefore consistent with the formal charge states of In^{3+} ($5s^0 5p^0$) and O^{2-} ($2p^6$), which explains the excellent correspondence between the classical and quantum energy landscapes. Electron density isosurfaces for three representative structures are shown in Fig. 6, which clearly reveal the nature of the HOMO and LUMO states. Of particular interest is the manifestation of the In 5*s* orbital as a lone pair-like state in the low symmetry coordination environments, which bears remarkable similarity to the asymmetric electron density associated with the filled s orbitals of Pb(II) and Sn(II);[42,43] the emergence of such states should facilitate the reduction of In(III) towards In(I) under appropriate chemical environments.

The single- and quasi- particle eigenvalues for the HOMO and LUMO levels of the ground state clusters for each n are plotted in Fig. 7. As expected, the eigenvalues resulting from the semi-local PBE functional result in a small HOMO–LUMO gap, and transition to the non-local PBE0 functional, which counters the self-interaction error and the energy derivative discontinuity present in the pure DFT functional,[44] opens the gap through both a significant lowering of the HOMO level and a raising of the LUMO level. Further application of the GW quasiparticle correction maintains the HOMO position of the PBE0 functional (to within 0.3 eV), but further raises the LUMO towards the vacuum level by 2.0–2.9 eV. The resulting quasiparticle ionisation potentials range from 8.1 to 7.1 eV ($\overline{IP} = 7.7$ eV), with electron affinities ranging from 0.7 to 2.10 eV ($\overline{EA} = 1.7$ eV).

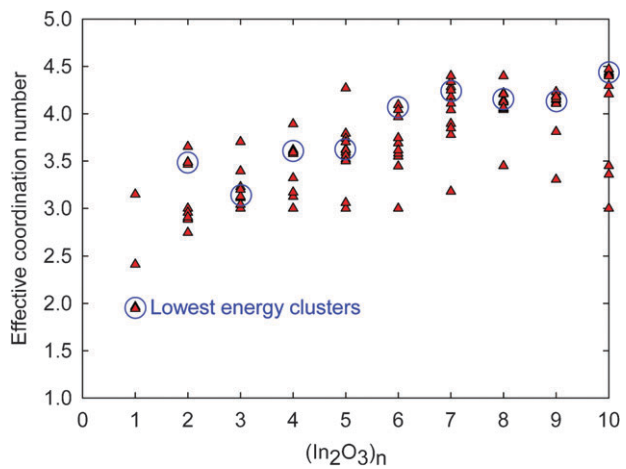

Fig. 5 The indium ion effective coordination numbers in each of the $(In_2O_3)_n$ nanoclusters, where the value for the lowest energy cluster is circled in blue for each n. The coordination numbers tend towards the bulk value of 6.

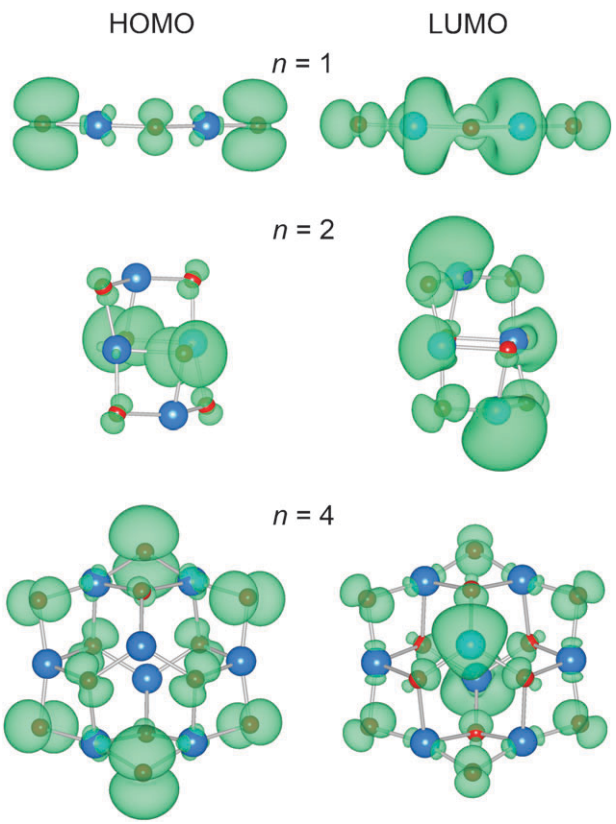

Fig. 6 Electron density isosurfaces for the HOMO and LUMO states of the ground state $(In_2O_3)_1$, $(In_2O_3)_2$ and $(In_2O_3)_4$ clusters.

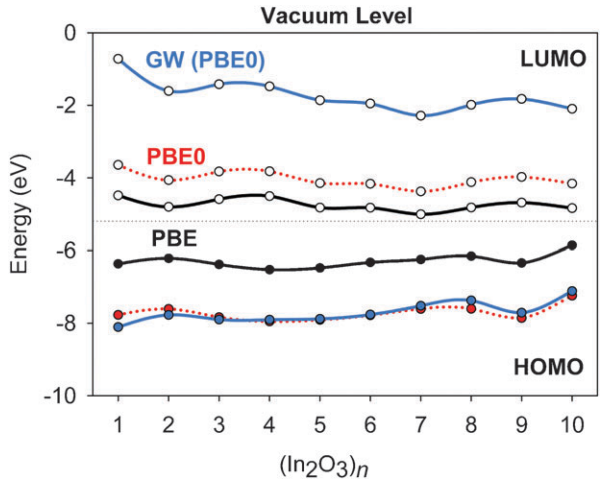

Fig. 7 Single- and quasi-particle eigenvalues for the HOMO and LUMO levels of the ground state In_2O_3 nanoclusters. The filled circles represent the HOMO state, while hollow circles represent the LUMO state. The energies are given relative to the vacuum level at 0 eV.

For bulk In_2O_3, the ionisation potentials and electron affinities have been the subject of recent experimental investigation. In the work of Klein *et al.*,[45] an ionisation potential of 7.1 eV was reported for polycrystalline In_2O_3 samples, which takes into account both the Moss-Burstein effect[46] (conduction band occupation) and the revised In_2O_3 band gap of 2.9 eV.[3] The bulk ionisation potential is remarkably close to our quasi-particle estimations, which is consistent with the asymmetry in the hole and electron effective masses of In_2O_3;[47] the lighter electron mass ($\sim$0.24 m_e) arising from the delocalised In 5*s* conduction band states results in much stronger quantum confinement effects compared to the more localised valence band states ($\sim$16 m_e) derived largely from O 2*p* orbitals. These results indicate that the electronic affinity should decrease monotonically as the LUMO level approaches the conduction band network of the bulk material. Thus, control of the nanocluster size during synthesis may allow for engineering of the electronic gap between 7 eV and 3 eV, which would be beneficial for applications in the deep UV range.

4. Conclusions

The lowest energy structures for a series of stoichiometric indium oxide nanoclusters have been predicted by combining a robust evolutionary algorithm with classical interatomic potential and quantum chemical models of the energy landscape. Both landscapes were found to give consistent low energy structures, with dense low symmetry nanoclusters favoured for molecular masses larger than $(In_2O_3)_5$. Electronic characterisation of the global minimum structures was performed at the PBE, PBE0 and GW levels of theory, with quasiparticle corrections found to be particularly important for correcting the electron affinities. These results provide initial insights into the nanochemistry of india, and experimental verification of these predictions would be most welcome.

Acknowledgements

We would like to thank Alexey Sokol, Stephen Shevlin and Richard Catlow for stimulating discussions. S.M.W. and A.W. would like to acknowledge funding from EPSRC (EP/F067496) and a Marie-Curie Intra-European Fellowship from the European Union under the Seventh Framework Programme, respectively. Materials Studio was kindly provided by Accelrys. Finally, in order to complete this work, we acknowledge that we made use of the UK's national high-performance computing service, HECToR, *via* our membership of the UK's HPC Materials Chemistry Consortium, which is also funded by EPSRC (EP/F067496).

References

1 P. P. Edwards, A. Porch, M. O. Jones, D. V. Morgan and R. M. Perks, *Dalton Trans.*, 2004, 2995–3002.
2 C. G. Granqvist and A. Hultaker, *Thin Solid Films*, 2002, **411**, 1.
3 A. Walsh, J. L. F. Da Silva, S.-H. Wei, C. Korber, A. Klein, L. F. J. Piper, A. DeMasi, K. E. Smith, G. Panaccione, P. Torelli, D. J. Payne, A. Bourlange and R. G. Egdell, *Phys. Rev. Lett.*, 2008, **100**, 167402.
4 A. Walsh, J. L. F. Da Silva, Y. Yan, M. M. Al-Jassim and S.-H. Wei, *Phys. Rev. B: Condens. Matter Mater. Phys.*, 2009, **79**, 073105.
5 T. Minami, T. Kakumu, Y. Takeda and S. Takata, *Thin Solid Films*, 1996, **290–291**, 1.
6 M. P. Taylor, D. W. Readey, M. F. A. M. v. Hest, C. W. Teplin, J. L. Alleman, M. S. Dabney, L. M. Gedvilas, B. M. Keyes, B. To, J. D. Perkins and D. S. Ginley, *Adv. Funct. Mater.*, 2008, **18**, 3169.
7 H. Hosono, M. Yasukawa and H. Kawazoe, *J. Non-Cryst. Solids*, 1996, **203**, 334–344.
8 A. Bourlange, D. J. Payne, R. M. J. Jacobs, R. G. Egdell, J. S. Foord, A. Schertel, P. J. Dobson and J. L. Hutchison, *Chem. Mater.*, 2008, **20**, 4551–4553.
9 A. Narayanaswamy, H. Xu, N. Pradhan, M. Kim and X. Peng, *J. Am. Chem. Soc.*, 2006, **128**, 10310–10319.
10 Q. Liu, W. Lu, A. Ma, J. Tang, J. Lin and J. Fang, *J. Am. Chem. Soc.*, 2005, **127**, 5276–5277.
11 A. Murali, A. Barve, V. J. Leppert, S. H. Risbud, I. M. Kennedy and H. W. H. Lee, *Nano Lett.*, 2001, **1**, 287–289.
12 C. H. Lee, M. Kim, T. Kim, A. Kim, J. Paek, J. W. Lee, S.-Y. Choi, K. Kim, J.-B. Park and K. Lee, *J. Am. Chem. Soc.*, 2006, **128**, 9326–9327.
13 S. M. Woodley, P. D. Battle, J. D. Gale and C. R. A. Catlow, *Phys. Chem. Chem. Phys.*, 1999, **1**, 2535–2542.
14 S. M. Woodley and R. Catlow, *Nat. Mater.*, 2008, **7**, 937–946.
15 J. D. Gale and A. L. Rohl, *Mol. Simul.*, 2003, **29**, 291–341.
16 A. A. Al-Sunaidi, A. A. Sokol, C. R. A. Catlow and S. M. Woodley, *J. Phys. Chem. C*, 2008, **112**, 18860–18875.
17 S. M. Woodley and C. R. A. Catlow, *Comput. Mater. Sci.*, 2009, **45**, 84.
18 C. R. A. Catlow, S. T. Bromley, S. Hamad, M. Mora-Fonz, A. A. Sokol and S. M. Woodley, *Phys. Chem. Chem. Phys.*, 2010, **12**, 786–811.
19 D. M. Deaven and K. M. Ho, *Phys. Rev. Lett.*, 1995, **75**, 288–291.
20 C. Roberts and R. L. Johnston, *Phys. Chem. Chem. Phys.*, 2001, **3**, 5024–5034.
21 A. Walsh, C. R. A. Catlow, A. A. Sokol and S. M. Woodley, *Chem. Mater.*, 2009, **21**, 4962–4969.
22 B. G. Dick and A. W. Overhauser, *Phys. Rev.*, 1958, **112**, 90.
23 G. Kresse and J. Furthmüller, *Phys. Rev. B: Condens. Matter*, 1996, **54**, 11169.
24 G. Kresse and J. Furthmüller, *Comput. Mater. Sci.*, 1996, **6**, 15.
25 J. P. Perdew, K. Burke and M. Ernzerhof, *Phys. Rev. Lett.*, 1996, **77**, 3865.
26 P. E. Blöchl, *Phys. Rev. B: Condens. Matter*, 1994, **50**, 17953.
27 V. Havu, V. Blum, P. Havu and M. Scheffler, *J. Comput. Phys.*, 2009, **228**, 8367–8379.

28 V. Blum, R. Gehrke, F. Hanke, P. Havu, V. Havu, X. Ren, K. Reuter and M. Scheffler, *Comput. Phys. Commun.*, 2009, **180**, 2175–2196.
29 E. van Lenthe, E. J. Baerends and J. G. Snijders, *J. Chem. Phys.*, 1994, **101**, 9783–9792.
30 M. Ernzerhof and G. E. Scuseria, *J. Chem. Phys.*, 1999, **110**, 5029–5036.
31 L. Hedin, *Phys. Rev.*, 1965, **139**, A796.
32 M. S. Hybertsen and S. G. Louie, *Phys. Rev. Lett.*, 1985, **55**, 1418.
33 H. Jiang, R. I. Gomez-Abal, P. Rinke and M. Scheffler, *Phys. Rev. Lett.*, 2009, **102**, 126403.
34 P. Rinke, A. Janotti, M. Scheffler and C. G. Van de Walle, *Phys. Rev. Lett.*, 2009, **102**, 026402.
35 S. M. Woodley, *Adapting global optimisation techniques for the prediction of microporous framework materials and small sized $(M_2O_3)_n$ nanoparticles in Novel Structural and Functional Materials and Methods for their Characterisation*, Kuprianova, Kiev, 2007.
36 J. Sun, W. C. Lu, W. Zhang, L. Z. Zhao, Z. S. Li and C. C. Sun, *Inorg. Chem.*, 2008, **47**, 2274–2279.
37 X. L. Ding, W. Xue, Y. P. Ma, Z. C. Wang and S. G. He, *J. Chem. Phys.*, 2009, **130**, 014303.
38 S. M. Woodley, S. Hamad, J. A. Mejias and C. R. A. Catlow, *J. Mater. Chem.*, 2006, **16**, 1927–1933.
39 S. M. Woodley, S. Hamad and C. R. A. Catlow, *Phys. Chem. Chem. Phys.*, 2010, DOI: 10.1039/c0cp00057d.
40 R. Hoppe, S. Voigt, H. Glaum, J. Kissel, H. P. Muller and K. Bernet, *J. Less Common Met.*, 1989, **156**, 105.
41 A. Walsh, J. L. F. Da Silva and S.-H. Wei, *Chem. Mater.*, 2009, **21**, 5119–5124.
42 D. J. Payne, R. G. Egdell, A. Walsh, G. W. Watson, J. Guo, P. A. Glans, T. Learmonth and K. E. Smith, *Phys. Rev. Lett.*, 2006, **96**, 157403.
43 A. Walsh and G. W. Watson, *J. Solid State Chem.*, 2005, **178**, 1422–1428.
44 L. J. Sham and M. Schlüter, *Phys. Rev. Lett.*, 1983, **51**, 1888.
45 A. Klein, C. Körber, A. Wachau, F. Säuberlich, Y. Gassenbauer, R. Schafranek, S. P. Harvey and T. O. Mason, *Thin Solid Films*, 2009, **518**, 1197.
46 T. S. Moss, *Proc. Phys. Soc., London, Sect. B*, 1954, **67**, 775.
47 A. Walsh, J. L. F. Da Silva and S.-H. Wei, *Phys. Rev. B: Condens. Matter Mater. Phys.*, 2008, **78**, 075211.